Platinum Decorated Gold Nanoparticles with Dual Functionalities for Ultrasensitive Colorimetric In Vitro Diagnostics

Zhuangqiang Gao,^{†,‡} Haihang Ye,[†] Dianyong Tang,[§] Jing Tao,^I Sanaz Habibi,[⊥] Adrienne Minerick,[⊥] Dianping Tang,[‡] and Xiaohu Xia^{†,*}

[†]Department of Chemistry, Michigan Technological University, Houghton, Michigan 49931, United States;

*Key Laboratory of Analysis and Detection for Food Safety (Fujian Province & Ministry of Education), Collaborative Innovation Center of Detection Technology for Haixi Food Safety and Products (Fujian Province), Department of Chemistry, Fuzhou University, Fuzhou 350108, People's Republic of China;

§International Academy of Targeted Therapeutics and Innovation, Chongqing University of Arts and Sciences, Chongqing 402160, People's Republic of China;

¹Condensed Matter Physics & Materials Science Department, Brookhaven National Laboratory, Upton, New York 11973, United States;

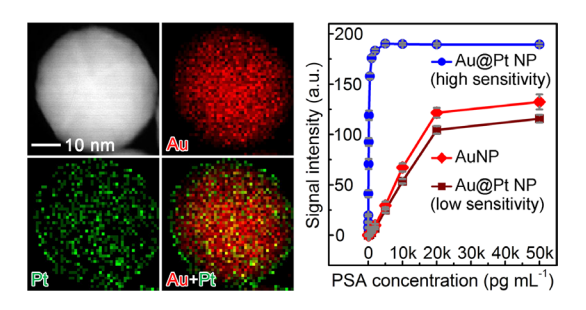
¹Department of Chemical Engineering, Michigan Technological University, Houghton, Michigan 49931, United States.

^{*}Corresponding author. E-mail: xiaxh@mtu.edu

Abstract

Au nanoparticles (AuNPs) as signal reporters have been utilized in colorimetric in vitro diagnostics (IVDs) for decades. Nevertheless, it remains a grand challenge to substantially enhance the detection sensitivity of AuNP-based IVDs as confined by the inherent plasmonics of AuNPs. In this work, we circumvent this confinement by developing a unique dual-functional AuNPs that were engineered by coating conventional AuNPs with ultrathin Pt skins of sub-10 atomic layers (*i.e.*, Au@Pt NPs). The Au@Pt NPs retain the plasmonic activity of initial AuNPs, while possess ultrahigh catalytic activity enabled by Pt skins. Such dual functionalities – plasmonics and catalysis – offer two different detection alternatives: one produced just by the color produced by plasmonics (low-sensitivity mode) and the second more sensitive color catalyzed from chromogenic substrates (high-sensitivity mode), achieving an "on-demand" tuning of the detection performance. Using lateral flow assay as a model IVD platform and conventional AuNPs as a benchmark, we demonstrate that the Au@Pt NPs could enhance detection sensitivity by two orders of magnitude.

Table of Contents



Keywords: In vitro diagnostics · gold nanoparticles · seeded growth · detection · biomarker

In vitro diagnostic (IVD) tests are crucial for patients and physicians to make timely and optimal decisions for patient care and treatment.¹⁻³ Colorimetric IVD, among many other types of IVD technologies, has received increasing attention in recent years due to its simplicity and cost effectiveness.⁴⁻¹⁰ The test results of colorimetric IVDs can be conveniently read out with the naked eyes and, if needed, quantified by an inexpensive and portable device.¹¹ In particular, these features make colorimetric IVDs extremely desirable for field work and point-of-care tests which are urgently needed, especially in resource-limited settings.

Au nanoparticles (AuNPs) as signal reporters have been widely used in colorimetric IVDs for decades because of their superior physicochemical properties.^{3,12} First, they offer highly intense color signals (red, in most cases) owing to an optical phenomenon called localized surface plasmon resonance (LSPR). 13-15 AuNPs of ~40 nm show an absorption cross-section 5 orders larger than ordinary organic dyes. 16 Second, they can be easily functionalized with biomolecules (e.g., antibodies and DNAs) by means of simple thiol-gold chemistry and/or electrostatic interactions. 17-20 Third, they are made of an inert noble metal and thus are highly stable, enabling them to survive harsh environments. Moreover, they can be easily and reproducibly synthesized in common chemical laboratories. The past few decades have witnessed a variety of AuNP-based IVD systems, with home pregnancy test being one of the most familiar examples.^{3,21-24} Despite the simplicity and practicality, it remains a challenge to substantially enhance the sensitivity of AuNP-based colorimetric IVDs without adding complexity. Note that high detection sensitivity is critical to many important applications such as early detection of cancers and infectious diseases, for which the concentrations of related biomarkers are very low.^{25,26} Since the detectable color signal in AuNP-based IVDs originates from the plasmonics of AuNPs, the detection sensitivity is essentially confined by the inherent plasmonic activity.

In this work, we report a novel strategy to circumvent such confinement of AuNP plasmonics and thus break through the detection limit barrier of associated colorimetric IVDs. Specifically, in this strategy, conventional AuNPs are decorated with conformal, thin skins of Pt to form unique Au@Pt_{nL} core@shell NPs (Figure 1a). The number (n) of Pt atomic layers could be precisely controlled in the range of 1-10. We demonstrated that, so long as the Pt shell is ultrathin (several atomic layers), the plasmonic property of the AuNP cores underneath Pt is well retained, making the resultant Au@Pt_{nL} NPs as red as the initial AuNPs (Figure 1b). On the other hand, Pt shells on the surface endow the Au@Pt_{nL} NPs with ultrahigh peroxidase-like catalytic activities,

allowing them to rapidly generate blue colored molecules by catalyzing the oxidation of 3,3',5,5'tetramethylbenzidine (TMB, a typical peroxidase substrate²⁷) by H₂O₂ in aqueous solution. It is worth mentioning that this catalytic reaction is extremely suitable for in vitro diagnostics and has been widely used in commercial diagnostic kits mainly because: i) both TMB and H₂O₂ are costeffective and non-toxic, ii) the reaction can be conveniently conducted in aqueous system and at room temperature, and iii) the blue colored product [i.e., oxidized TMB (oxTMB) with λ_{max} = 653 nm] has a large molar extinction coefficient.²⁷ Significantly, the intensity of blue color from catalysis is orders of magnitude stronger than that of the intrinsic red color from plasmonics, ensuring an enhanced detection sensitivity. These dual functionalities – plasmonics and catalysis – of the Au@Pt_{nL} NPs make them particularly suitable for colorimetric IVDs. They can offer two different detection alternatives: one produced just by the red color of interior AuNPs (lowsensitivity mode) and the second more sensitive blue color produced by the Pt shell through catalysis (high-sensitivity mode), achieving an "on-demand" tuning of the detection performance. It should be pointed out that the low-sensitivity mode is faster and more convenient than the high-sensitivity mode because the latter involves an additional signal enhancement procedure (i.e., 5-minute TMB/H₂O₂ treatment process, see Supporting Information for details). In practical use, one will first perform the low-sensitivity mode. High-sensitivity mode is only needed when no signal is observed in low-sensitivity mode (for samples with low concentration of analytes or negative samples). Using lateral flow assay as a model IVD system, we demonstrated that the detection sensitivity could be enhanced by ~100 times as compared to conventional AuNPs as the benchmark.

We started with the synthesis of Au@Pt_{nL} NPs that was conducted using seed-mediated growth. In a standard synthesis, an aqueous solution of Na₂PtCl₆ as precursor to Pt was injected slowly (1.2 mL/h, with a syringe pump) into a mixture containing ~40 nm citrate-capped AuNPs with an overall spherical shape as the seeds, L-ascorbic acid as a reductant, and sodium citrate as a colloidal stabilizer, which had been preheated to 90 °C under magnetic stirring (see Supporting Information for details). We chose ~40 nm citrate-capped AuNPs as a model seed because they have been extensively used for various IVD systems.²⁸⁻³¹ As shown by the transmission electron microscopy (TEM) images in Figure S1, the Au seeds displayed uniform spherical shapes and smooth surfaces. Most of them contained multiply twinned defects. Their average diameter was measured to be 40.2 nm by randomly analyzing 200 particles. Figure 2a and 2b, respectively,

show typical low- and high-magnification TEM images of the Au@Pt_{nL} NPs prepared from a standard synthesis. It can be seen that the spherical shape, smooth surface, and twin structures of the Au seeds were well retained after Pt growth, implying the involvement of a layer-by-layer growth mode. The average edge length of the Au@Pt_{nL} NPs was measured to be 42.1 nm, which was 1.9 nm greater than that of the initial Au seeds. Therefore, on average, the thickness of the Pt shell deposited on the Au spherical seed was about 0.95 nm. Figure 2c shows a high-angle annular dark-field scanning TEM (HAADF-STEM) image of the same sample, from which the 3D spherical shape and smooth surface were more evident relative to the TEM images. The high-resolution TEM image of an individual particle (Figure 2d) reveals the continuous lattice fringes from Au core to Pt shell, indicating an epitaxial relationship between these two metals.

Since Au and Pt have similar atomic masses and lattice constants, it is almost impossible to resolve Pt from Au via electron microscopy.³² As such, the elemental distribution of Au and Pt in the sample was determined by energy-dispersive X-ray (EDX) mapping and line-scans analyses. From the EDX mapping image (Figure 2e), Au could only be observed in the interior (red) while Pt was distributed across the entire particle including the shell (green), suggesting an Au@Pt core@shell structure and the conformal coating of Pt on Au surface. The core@shell structure was further confirmed by the EDX line-scan profile recorded along a central axis direction of an individual sphere (Figure 2f), where the Pt trace dominated the shell region. To further confirm Pt was conformally distributed on Au surfaces, those Au@Pt_{nL} NPs were etched with a chemical etchant, of which strength is sufficiently strong to etch Au while too weak to react with Pt.33 As shown by the TEM images in Figure S2, most of the Au@Pt_{nL} NPs were intact after etching. Only ~2% of them was converted to thin nanoshells with a hollow interior. This result suggested that conformal Pt overlayers existed in most of the Au@Pt_{nL} NPs, which prevented the Au cores from being etched. For a small portion of Au@Pt_{nL} NPs that were not fully covered by Pt, Au cores were etched away, leaving only nanoshells of Pt. The surface properties of the Au@Pt_{nL} NPs were determined by X-ray photoelectron spectroscopy (XPS). It can be seen that the XPS survey spectrum of the Au@Pt_{nL} NPs was similar to that of the initial Au seeds, except for the appearance of Pt characteristic peaks (Figure 2g). This observation suggests that the surface ligands on AuNPs remain unchanged after they had been coated with Pt, which ensured the simplicity of antibody functionalization as discussed later. The high-resolution spectra of the Pt 4f peaks (Figure 2h) revealed the existence of three chemical states for Pt species, where the Pt⁰ was dominant.

To quantitatively determine the average number (*n*) of Pt atomic layers for the Au@Pt_{nL} NPs shown in Figure 2, the sample was subject to inductively coupled plasma-optical emission spectrometry (ICP-OES) analysis. The mass ratio of Au to Pt was measured to be 6.49:1. According to this ICP-OES data, the size of Au spherical seeds, and the densities of Au and Pt, the thickness of Pt shell was quantified to be 0.89 nm (see Figure S3 for details), which is in good agreement with the value of 0.95 nm measured from the change to average diameter by TEM. In the following discussion, Pt shell thickness is referred to the data from ICP-OES because it averages over a much larger number of particles than TEM. Since a nanosphere of face-centered cubic structure tends to expose low-energy (111) surfaces, ^{34,35} for rough estimation, here we assume Pt layers are spaced by Pt{111} planes with the interplanar distance of ~0.23 nm. ^{36,37} Thus, the average number of Pt atomic layers was ~4 for this sample, so is denoted as Au@Pt_{4L} NPs.

As demonstrated in our previous studies, $^{38-41}$ so long as the deposition of Pt on Au was directed to follow a layer-by-layer mode, the thickness of the Pt shells could be conveniently controlled with atomic precision by simply adjusting the amount of Pt precursor introduced to the synthesis. The key to induce and maintain such layer-by-layer mode was to ensure a slow atom deposition relative to surface diffusion ($V_{\text{dep.}} < V_{\text{diff.}}$, see Figure 1a) so the Pt adatoms could spread across the entire Au surface, resulting in the formation of a conformal and smooth Pt coating. This argument was supported by our experimental result that Pt dendrites (Figure S4), instead of smooth shells, were formed on Au seeds when the atom deposition rate was raised by increasing the injection rate of Pt precursor while all other conditions were kept unchanged. With this mechanistic understanding, we were able to finely tune the thickness of Pt shells from 1 to 10 atomic layers that were confirmed by both electron microscopy imaging and ICP-OES analysis (see Supporting Information and Table S1 for experimental details). For example, Au@Pt_{2L} NPs (Figure S5a) and Au@Pt_{7L} NPs (Figure S5b), respectively, could be obtained by adjusting the amount of Pt precursor from 347 μ L in a standard synthesis to 170 and 628 μ L.

We then evaluated the plasmonic properties of the Au@Pt_{nL} NPs (n = 0-10). Here, Au@Pt_{0L} NPs correspond to the initial AuNP seeds. Figure 3a compares the appearance of aqueous suspensions of Au@Pt_{nL} NPs and initial Au seeds with the same particle concentration. An overall red color can be seen for all the samples, while the color intensity decreased with the

increase of Pt atomic layers. Figure 3b shows the corresponding UV-vis spectra recorded from these samples. As the number (n) of Pt layers increased, the major LSPR peak at ~520 nm broadened, together with an intensity decrease. Compared to initial Au seeds, the extinction at 520 nm for the Au@Pt_{nL} NPs was decreased by ~11% and ~15%, respectively, when n = 2 and 4 (see inset of Figure 3b). At n = 10, the decrease was enlarged to ~20%. Further increase of the Pt shell thickness led to the diminishment and eventual disappearance of the characteristic red color. For instance, the red color is barely detectable when the thickness of Pt shell reached 10 nm (ca. 44 Pt atomic layers, see Figure S6). These data demonstrate that the ultrathin coating of Pt (preferably several atomic layers) is critical to the retaining of plasmonic properties.

The peroxidase-like catalytic property of Au@Pt_{nL} NPs was investigated with the oxidation of TMB by H₂O₂ being as a model catalytic reaction. ⁴²⁻⁴⁴ As shown in Figure 3c, Au@Pt_{nL} NPs could rapidly generate a blue-colored product (*i.e.*, oxTMB) through the catalytic reaction. The intensity of blue color increased as the number (*n*) of Pt layers increased and became saturated at n = 4. In contrast, the initial AuNPs (*i.e.*, Au@Pt_{0L} NPs) could barely catalyze the reaction (see Figure 3c). To quantify the catalytic efficiency, catalytic constant (K_{cat} , defined as the maximum number of colored molecules generated per second per catalyst) was determined through the apparent steady-state kinetic assay (see Supporting Information and Figure S7 for details). ^{42,45} As summarized by Figure 3d, K_{cat} for the Au@Pt_{nL} NPs ($n \ge 4$) reached the regime of 10⁶ s⁻¹, which is several orders of magnitudes higher than those of the initial AuNPs and natural peroxidases. ⁴²

To better understand the relationship between the structure of Au@Pt_nL NPs and their plasmonic and catalytic properties, we conducted preliminary theoretical calculations. We first performed finite-difference time-domain (FDTD) simulations to investigate the extinction cross-section spectra of Au@Pt_nL NPs (n = 0-10, see Supporting Information for detailed methods). The simulation results are shown in Figure S8. It can be seen that the AuNP seeds displayed a major LSPR peak at ~532 nm. When they were coated with Pt of different atomic layers (n), their LSPR peak gradually blue-shifted and broadened as n increased. The peak intensity decreased rapidly as n increased from 0 to 4. Thereafter (n = 5-10), the decrease of peak intensity slowed down. The overall trends of the changes in LSPR peak position, shape, and intensity agreed well with the experimental results shown in Figure 3b. In order to gain insight into the peroxidase-like catalytic activities of those Au@Pt_nL NPs, we performed density functional theory (DFT) calculations to study the surface electronic structures of Pt overlayers on Au

surface, where the d-band center positions were derived (see Supporting Information for detailed methods). It is well documented that the d-band center of surface atoms of a transition-metal catalyst is a good measurement for its binding affinity toward adsorbates and therefore its catalytic activity. ⁴⁷⁻⁵⁰ Figure S9a shows the partial density of state (PDOS) profiles of 5d-orbitals for the outmost atoms of Au(111) and Au@Pt_{nL}(111) (n = 1-10) surfaces. It can be seen that the d-band of Au(111) surface was narrower and had a much lower density near the Fermi level compared to those of Au@Pt_{nL}(111) surfaces. These results indicated that Au(111) was less catalytically active than Au@Pt_{nL}(111) surfaces, ^{51,52} which is in good agreement with the experimental results shown in Figure 3c, d. For the Au@Pt_{nL}(111) surfaces with n = 1-10, significant change of d-band center positions was only observed when n increased from 1 to 3 (see Figure S9b), suggesting that the change of catalytic activity of Au@Pt_{nL}(111) should be obvious in the range of n = 1-3. ⁴⁷ This result is in line with the experimental observations that the catalytic activity of Au@Pt_{nL} NPs drastically increased as n increased from 1 to 3 and tended to become saturated when $n \ge 4$ (see Figure 3d).

It should be emphasized that, even though Au@Pt core@shell nanostructures have been extensively reported in literature,⁵³⁻⁵⁷ most of those studies did not precisely control over the surface structure and shell thickness at the atomic level. Particularly, in most cases, the deposition of Pt on Au seeds was not maintained along a layer-by-layer mode during the entire course of growth.⁴⁰ As a result, Pt shells in the final products oftentimes took irregular morphologies. In the present work, Pt shells with a well-defined morphology and thickness of 1-10 atomic layers were successfully coated on Au seeds, which allowed us to systematically investigate the structure-property relationships from both experimental and theoretical angles. We believe the insights from this study will serve as a strong foundation to inspire future work.

Since n = 4 for the Au@Pt_{nL} NPs well balanced the decrease of plasmonic activity and the increase of catalytic activity, the Au@Pt_{4L} NPs (Figure 2) were chosen for subsequent studies. It should be emphasized that the intensity of blue color from catalysis was significantly higher than that of the intrinsic red color from plasmonics. Specifically, the molar extinction coefficient of the 40.2 nm AuNPs was determined to be ~9.5×10⁹ M⁻¹ cm⁻¹ (see Figure S10 for details), which is consistent with literature reports on 40 nm AuNPs. ^{16,58,59} In contrast, the equivalent molar extinction coefficient (defined as the total light extinction of colored products catalyzed at t = 5 min) of the Au@Pt_{4L} NPs was calculated to be ~1.8×10¹³ M⁻¹ cm⁻¹ (see Figure S10 for details).

To our knowledge, this value represents the record-high extinction coefficient among all types of nanoparticles with similar sizes. Taken together, the color signal of ~40 nm AuNPs could be enhanced by 3 orders of magnitude through a simple substrate treatment process (5 min, room temperature, and aqueous system), which forms the basis for exceptional detection sensitivity. Notably, this enhancement is expected to be more evident for AuNPs of smaller sizes since the molar extinction of AuNPs decreases at a fast rate proportional to the cube of particle radius.⁶⁰

Finally, we applied the Au@Pt_{4L} NPs to lateral flow assay (LFA) of human prostate-specific antigen (PSA) as a model cancer biomarker, 61 according to the principle shown in Figure 4a (experimental details in Supporting Information). LFA is one of a handful of point-of-care techniques that can claim to have taken tests out of the laboratory. 62-65 AuNPs with tens of nanometers in size have been widely used in LFA as colorimetric labels for decades because of their superior physicochemical properties.^{22,66} While creative research effort continues to be invested into the improvement in detection performance for AuNP-based LFAs, there is still an unmet need for a broadly applicable methodology to provide ultra-low detection limits. A transformative idea to enhance the detection sensitivity of LFA is to amplify the plasmonics of AuNPs. The most commonly used strategy for plasmonics amplification is to assemble numerous AuNPs on larger sized carrier particles. For example, Xu and co-workers decorated silica rods of several micrometers with AuNPs. 67 ~104 AuNPs were assembled on a single silica rod. Owing to the increased AuNP density, the detection limit was lowered more than ten times compared to conventional AuNP based LFA. Similarly, branched dendrimers as carriers also displayed enhanced color intensity.⁶⁸ Despite these demonstrations, this strategy is limited by the loading capacity of a carrier and the bulkiness of the AuNPs-carrier complexes, which inhibit the particle's migration within the strip thus exacerbating the steric effect for bioreceptor binding to analytes. Another notable strategy for plasmonics amplification is to enlarge the AuNPs on the test line through post gold or silver enhancement, in which the size and thus optical intensity of AuNPs is increased. ⁶⁹⁻⁷¹ This strategy is troubled by using large amounts of highly toxic Au³⁺ or Ag⁺ ions. Both ions adversely affect the environment and have serious biological effects on human health. 72-74 Unless this issue can be addressed, it will be impractical to implement this method into LFAs, especially in non-laboratory scenarios. Taken together, it remains a challenge to substantially enhance the sensitivity of AuNP-based LFAs that are presently confined by the inherent plasmonics of AuNPs.

For direct comparison, we benchmarked the performance of Au@Pt_{4L} NPs in LFA against initial ~40 nm AuNPs by using the same set of antibodies and materials. Procedures for the Au@Pt_{4L} NP- and AuNP-based LFAs were also kept the same except that an additional enhancement procedure (*i.e.*, TMB/H₂O₂ treatment) was involved in the "high-sensitivity" Au@Pt_{4L} NP-LFA (see Figure 4a). It is worth noting that Au@Pt_{4L} NPs could be easily functionalized with antibodies through a simple incubation process as what is usually used for conventional AuNPs (see Supporting Information and Figure S11 for details).^{75,76} This facile antibody functionalization of Au@Pt_{4L} NPs could be ascribed to the existence of similar ligands on the surfaces as conventional AuNPs that had been demonstrated by the XPS data shown in Figure 2g.

PSA standards with various concentrations were monitored in test strips. The detection results were recorded with a digital camera (Figure 4b) and were subject to quantification using Adobe Photoshop software (Figure 4c). It can be seen that intensities of red bands at the test line region for both AuNP- and Au@Pt_{4L} NP-LFAs ("low-intensity mode") were almost the same. The naked eye detection limit was about 2 ng mL⁻¹ of PSA for both LFAs. This result suggests that the Au@Pt_{4L} NPs could be utilized in the same fashion as conventional AuNPs without the compromise of performance. For Au@Pt4L NP-LFA at the "high-intensity mode", blue/purple lines could be resolved for strips applied with PSA standards of concentrations as low as 20 pg mL⁻¹. It should be mentioned that a faint blue color was observed for the zero calibrator under high-sensitivity mode. This background signal may be caused by the non-specific binding of a small amount of Au@Pt_{4L} NPs to the test line region, which were capable of catalyzing the formation of visible blue colored oxTMB molecules. Figure 4c compares the calibration curves of the three LFAs that were generated by plotting the color intensity at test line against the PSA concentration. In particular, a quality linear relationship ($R^2 = 0.996$) in the range of 10-200 pg mL⁻¹ PSA was observed for the "high-sensitivity" Au@Pt4L NP-LFA (inset of Figure 4c). The detection limit, defined as the concentration corresponding to a signal that is 3 times the standard deviation above the zero calibrator, 77,78 was calculated to be 3.1 pg mL⁻¹ for the "highsensitivity" Au@Pt4L NP-LFA. It is worth pointing out that this detection limit is even lower than what could be achieved by commercial enzyme-linked immunosorbent assay (ELISA) kit (4.9 pg mL⁻¹, Abcam plc., United Kingdom, see Figure S12), which involves complicated operation procedures and instruments. In comparison, the detection limits of the AuNP-LFA and "lowsensitivity" Au@Pt_{4L} NP-LFA were determined to be 272 and 322 pg mL⁻¹, respectively, based on their calibration curves (Figure 4c). These results demonstrated that Au@Pt_{4L} NP could enhance the sensitivity of conventional LFA by ~100 times, enabling it to rival the sensitivities of other sophisticated instrument-based IVD techniques (*e.g.*, ELISA). Such a significant enhancement in sensitivity is only paid by a simple, 5-min substrate treatment process at room temperature. It should be mentioned that the magnitude of color signal enhancement by Au@Pt_{4L} NPs relative to conventional AuNPs in LFA test (~100 times, Figure 4) was lower than the case when Au@Pt_{4L} NPs were suspended in aqueous solution (~1,000 times, see Figure 3 and Figure S10). Note, in LFA test, Au@Pt_{4L} NPs were immobilized and accumulated on solid phase (*i.e.*, nitrocellulose the membrane of test strip). Therefore, the relatively low signal enhancement in LFA test can be ascribed to the compromise of catalytic activity of Au@Pt_{4L} NPs that was caused by the facts that: *i*) the same nanocatalysts-medicated catalytic reaction in a solid-solution phase is generally less effective than in a solution phase;⁷⁹ and *ii*) the aggregation of Au@Pt_{4L} NPs in LFA test strips reduced the total surface area of active Pt surface.

We also compared the performance of Au@Pt_{4L} NPs in LFA of PSA standards with those of Pt dendrites coated AuNPs (i.e., the sample shown in Figure S4, which will be referred to as "Au@Ptdendrite NPs") and PtNPs (see Figure S13) with similar sizes and the same surface ligands (i.e., citrate). In the comparisons, all experimental conditions were kept unchanged except for the substitution of Au@Pt4L NPs with the same amount of Au@Ptdendrite NPs or PtNPs. As shown in Figure S14, the detection sensitivity of Au@Ptdendrite NP-LFA was comparable to that of Au@PtdL NP-LFA in both low- and high-sensitivity modes. PtNPs were synthesized according to a previously reported procedure with slight modifications.⁸⁰ As shown by the TEM image in Figure S13, the PtNPs displayed relatively irregular surface and broad size distribution compared to the Au@Pt4L NPs. Figure S15 shows the performance of those PtNPs in LFA of PSA standards. It can be seen that the detection sensitivity of PtNP-LFA was similar to that of Au@Pt_{4L} NP-based LFA under high-sensitivity mode. However, under low-sensitivity mode, its detection sensitivity was several times lower than Au@Pt4L NP-LFA. This difference can be ascribed to the fact that Au@Pt4L NPs with Au cores possess superior optical properties relative to the PtNPs of similar size.⁸¹ It should be emphasized that the Au@Pt_{nL} NPs presented in this work are much more uniform, in terms of size, shape, and elemental distribution, than the Au@Ptdendrite NPs and PtNPs. Accordingly, they are expected to provide better detection

reproducibility.⁸² In addition, their properties (*e.g.*, plasmonic and catalytic activities) were well understood at the atomic level. Therefore, we believe the Au@Pt_{nL} NPs are more suitable for biosensing applications, providing sensitive and reliable tests.

To demonstrate the potential clinical use of the "high-sensitivity" Au@Pt4L NP-LFA, we applied it to quantifying PSA from human plasma samples (from a healthy female donor, provided by the UP Health System-Portage, Houghton, Michigan, United States) that had been spiked with PSA at concentrations of 20-160 pg mL⁻¹. The detection was benchmarked against a commercial ELISA kit. As summarized in Table 1, the analytical recoveries for Au@Pt4L NP-LFA in analyzing the five PSA spiked human plasma samples were determined to be in the range of 94.5-106.6%. The coefficient of variation (n = 6) for all samples was below 7.3%. The detection results correlated well with the parallel tests by commercial ELISA kit with a correlation coefficient $R^2 = 0.992$ (see Table 1 and Figure S16). These data demonstrated that the performance of Au@Pt4L NP-LFA was not influenced by the complex matrices in human plasma, suggesting the feasibility of the new LFA in analyzing clinical samples.

In summary, we have demonstrated a dual-functional AuNPs (with both plasmonic and catalytic activities) for colorimetric in vitro diagnostics with substantially enhanced detection sensitivity. Such dual-functional AuNPs were engineered by coating conventional AuNPs with ultrathin Pt skins of sub-10 atomic layers (*i.e.*, Au@Pt NPs). The enhanced sensitivity is ascribed to the ultrahigh catalytic activity of the Au@Pt NPs that allows them to generate detectable color signal orders of magnitude stronger than the intrinsic color from plasmonics. Importantly, the Au@Pt NPs retain all the merits of conventional AuNPs, making it convenient and straightforward to employ them for clinical diagnostics.

ASSOCIATED CONTENT

Supporting Information

Information on materials, methods, experimental details, additional images, tables, schematics, spectra, and plots is available free of charge via the Internet at http://pubs.acs.org.

AUTHOR INFORMATION

Corresponding Author

*E-mail: xiaxh@mtu.edu (X. Xia)

Notes

The authors declare no competing financial interest.

ACKNOWLEDGMENTS

This work was supported in part by the startup funds from Michigan Technological University and a National Science Foundation (NSF) Career Award (CHE-1651307). Part of the electron microscopy work at Brookhaven National Laboratory was supported by the U.S. Department of Energy, Basic Energy Sciences, Division of Materials Science and Engineering, under Contract no. DE-SC0012704.

REFERENCES

- (1) Gottlieb, S.; Woodcock, J. Nat. Biotech. 2006, 24, 927-929.
- (2) Giljohann, D. A.; Mirkin, C. A. *Nature* **2009**, *462*, 461-464.
- (3) Zhou, W.; Gao, X.; Liu, D.; Chen, X. Chem. Rev. 2015, 115, 10575-10636.
- (4) Elghanian, R.; Storhoff, J. J.; Mucic, R. C.; Letsinger, R. L.; Mirkin, C. A. Science 1997, 277, 1078-1081.
- (5) Li, H.; Rothberg, L. J. J. Am. Chem. Soc. **2004**, 126, 10958-10961.
- (6) Cheng, C. M.; Martinez, A. W.; Gong, J.; Mace, C. R.; Phillips, S. T.; Carrilho, E.; Mirica, K. A.; Whitesides, G. M. *Angew. Chem., Int. Ed.* **2010**, *49*, 4771-4774.
- (7) Qu, W.; Liu, Y.; Liu, D.; Wang, Z.; Jiang, X. Angew. Chem., Int. Ed. **2011**, 50, 3442-3445.
- (8) Zhu, Z.; Wu, C.; Liu, H.; Zou, Y.; Zhang, X.; Kang, H.; Yang, C. J.; Tan, W. *Angew. Chem., Int. Ed.* **2010**, *49*, 1052-1056.
- (9) De La Rica, R.; Stevens, M. M. *Nat. Nanotechnol.* **2012**, *7*, 821-824.
- (10) Fu, X.; Chen, L.; Choo, J. Anal. Chem. 2017, 89, 124-137.
- (11) Martinez, A. W.; Phillips, S. T.; Carrilho, E.; Thomas III, S. W.; Sindi, H.; Whitesides, G. M. Anal. Chem. 2008, 80, 3699-3707.
- (12) Huang, X.; El-Sayed, M. A. J. Adv. Res. **2010**, 1, 13-28.
- (13) Eustis, S.; El-Sayed, M. A. Chem. Soc. Rev. 2006, 35, 209-217.

- (14) Willets, K. A.; Van Duyne, R. P. Annu. Rev. Phys. Chem. 2007, 58, 267-297.
- (15) Mayer, K. M.; Hafner, J. H. Chem. Rev. 2011, 111, 3828-3857.
- (16) Jain, P. K.; Lee, K. S.; El-Sayed, I. H.; El-Sayed, M. A. J. Phys. Chem. B 2006, 110, 7238-7248.
- (17) Love, J. C.; Estroff, L. A.; Kriebel, J. K.; Nuzzo, R. G.; Whitesides, G. M. *Chem. Rev.* **2005**, *105*, 1103-1170.
- (18) Cao-Milán, R.; Liz-Marzán, L. M. Expert Opin. Drug Delivery 2014, 11, 741-752.
- (19) Kumar, S.; Aaron, J.; Sokolov, K. Nat. Protoc. 2008, 3, 314-320.
- (20) Sokolov, K.; Follen, M.; Aaron, J.; Pavlova, I.; Malpica, A.; Lotan, R.; Richards-Kortum, R. Cancer Res. 2003, 63, 1999-2004.
- (21) Saha, K.; Agasti, S. S.; Kim, C.; Li, X.; Rotello, V. M. Chem. Rev. 2012, 112, 2739-2779.
- (22) Posthuma-Trumpie, G. A.; Korf, J.; van Amerongen, A. *Anal. Bioanal. Chem.* **2009**, *393*, 569-582.
- (23) Huang, X.; Jain, P. K.; El-Sayed, I. H.; El-Sayed, M. A. Nanomedicine 2007, 2, 681-693.
- (24) Sun, J.; Xianyu, Y.; Jiang, X. Chem. Soc. Rev. 2014, 43, 6239-6253.
- (25) Perfézou, M.; Turner, A.; Merkoçi, A. Chem. Soc. Rev. 2012, 41, 2606-2622.
- (26) Wu, L.; Qu, X. Chem. Soc. Rev. 2015, 44, 2963-2997.
- (27) Josephy, P. D.; Eling, T.; Mason, R. P. J. Biol. Chem. 1982, 257, 3669-3675.
- (28) Ching, K. H. Lateral Flow Immunoassay. In *ELISA: Methods and Protocols*, Hnasko, R. Ed. Springer New York: New York, NY, 2015; 127-137.
- (29) Choi, D. H.; Lee, S. K.; Oh, Y. K.; Bae, B. W.; Lee, S. D.; Kim, S.; Shin, Y.-B.; Kim, M.-G. Biosens. Bioelectron. 2010, 25, 1999-2002.
- (30) Nath, N.; Chilkoti, A. Anal. Chem. 2004, 76, 5370-5378.
- (31) Liu, X.; Wang, Y.; Chen, P.; McCadden, A.; Palaniappan, A.; Zhang, J.; Liedberg, B. *ACS Sens.* **2016**, *1*, 1416-1422.
- (32) Bian, T.; Zhang, H.; Jiang, Y.; Jin, C.; Wu, J.; Yang, H.; Yang, D. *Nano Lett.* **2015**, *15*, 7808-7815.
- (33) Jiang, H.-J.; Ham, S.; Acapulco, J. A.; Song, Y.; Hong, S.; Shuford, K. L.; Park. S. *J. Am. Chem. Soc.* **2014**, *136*, 17674-17680.
- (34) Xia, Y.; Xiong, Y.; Lim, B.; Skrabalak, S. E. Angew. Chem., Int. Ed. 2009, 48, 60-103.
- (35) Xia, Y.; Gilroy, K. D.; Peng, H.-C.; Xia, X. Angew. Chem., Int. Ed. 2017, 56, 60-95.

- (36) Song, H.; Kim, F.; Connor, S.; Somorjai, G. A.; Yang, P. J. Phys. Chem. B **2005**, 109, 188-193.
- (37) Jiang, K.; Zhao, D.; Guo, S.; Zhang, X.; Zhu, X.; Guo, J.; Lu, G.; Huang, X. Sci. Adv. **2017**, *3*, e1601705.
- (38) Xia, X.; Xie, S.; Liu, M.; Peng, H.-C.; Lu, N.; Wang, J.; Kim, M. J.; Xia, Y. *Proc. Natl. Acad. Sci. U.S.A.* **2013**, *110*, 6669-6673.
- (39) Xia, X.; Figueroa-Cosme, L.; Tao, J.; Peng, H.-C.; Niu, G.; Zhu, Y.; Xia, Y. *J. Am. Chem. Soc.* **2014**, *136*, 10878-10881.
- (40) Xia, Y.; Xia, X.; Peng, H.-C. J. Am. Chem. Soc. 2015, 137, 7947-7966.
- (41) Ye, H.; Wang, Q.; Catalano, M.; Lu, N.; Vermeylen, J.; Kim, M. J.; Liu, Y.; Sun, Y.; Xia, X. *Nano Lett.* **2016**, *16*, 2812-2817.
- (42) Gao, L.; Zhuang, J.; Nie, L.; Zhang, J.; Zhang, Y.; Gu, N.; Wang, T.; Feng, J.; Yang, D.; Perrett, S. *Nat. Nanotechnol.* **2007**, *2*, 577-583.
- (43) Xia, X.; Zhang, J.; Lu, N.; Kim, M. J.; Ghale, K.; Xu, Y.; McKenzie, E.; Liu, J.; Ye, H. *ACS Nano* **2015**, *9*, 9994-10004.
- (44) Porter, D.; Bright, H. J. Biol. Chem. 1983, 258, 9913-9924.
- (45) Wei, H.; Wang, E. Chem. Soc. Rev. 2013, 42, 6060-6093.
- (46) Jiang, R.; Chen, H.; Shao, L.; Li, Q.; Wang, J. Adv. Mater. 2012, 24, OP200-OP207.
- (47) Nørskov, J. K.; Bligaard, T.; Hvolbæk, B.; Abild-Pedersen, F.; Chorkendorff, I.; Christensen, C. H. *Chem. Soc. Rev.* **2008**, *37*, 2163-2171.
- (48) Greeley, J.; Nørskov, J. K.; Mavrikakis, M. Annu. Rev. Phys. Chem. 2002, 53, 319-348.
- (49) Zhang, J.; Vukmirovic, M. B.; Xu, Y.; Mavrikakis, M.; Adzic, R. R. Angew. Chem., Int. Ed. **2005**, 44, 2132-2135.
- (50) Nørskov, J. K.; Bligaard, T.; Rossmeisl, J.; Christensen, C. H. Nat. Chem. 2009, 1, 37-46.
- (51) Sholl, D. S.; Steckel, J. A. *Density Functional Theory: A Practical Introduction*; John Wiley & Sons, Inc.: Hoboken, NJ, **2009**.
- (52) Mirkin, M. V.; Amemiya, S. *Nanoelectrochemistry*; CRC Press: Boca Raton, FL, **2014**.
- (53) Xie, W.; Herrmann, C.; Kömpe, K.; Haase, M.; Schlücker, S. *J. Am. Chem. Soc.* **2011**, *133*, 19302-19305.
- (54) Kang, S. W.; Lee, Y. W.; Park, Y.; Choi, B.-S.; Hong, J. W.; Park, K.-H.; Han, S. W. ACS Nano 2013, 7, 7945-7955.

- (55) Guo, S.; Li, J.; Dong, S.; Wang, E. J. Phys. Chem. C 2010, 114, 15337-15342.
- (56) Fu, Q.; Wu, Z.; Du, D.; Zhu, C.; Lin, Y.; Tang, Y. ACS Sens. 2017, 2, 789-795.
- (57) Varadea, D.; Haraguchi, K. Chem. Commun. 2014, 50, 3014-3017.
- (58) Haiss, W.; Thanh, N. T. K.; Aveyard, J.; Fernig, D. G. Anal. Chem. 2007, 79, 4215-4221.
- (59) Liu, X.; Atwater, M.; Wang, J.; Huo, Q. Colloids Surf. B 2007, 58, 3-7.
- (60) Yang, X.; Yang, M.; Pang, B.; Vara, M.; Xia, Y. Chem. Rev. 2015, 115, 10410-10488.
- (61) Lilja, H.; Ulmert, D.; Vickers, A. J. Nat. Rev. Cancer 2008, 8, 268-278.
- (62) Weigl, B.; Domingo, G.; LaBarre, P.; Gerlach, J. Lab Chip 2008, 8, 1999-2014.
- (63) Yager, P.; Domingo, G. J.; Gerdes, J. Annu. Rev. Biomed. Eng. 2008, 10, 107-144.
- (64) McNerney, R.; Daley, P. Nat. Rev. Microbiol. 2011, 9, 204-213.
- (65) Gubala, V.; Harris, L. F.; Ricco, A. J.; Tan, M. X.; Williams, D. E. *Anal. Chem.* **2012**, *84*, 487-515.
- (66) Quesada-González, D.; Merkoçi, A. Biosens. Bioelectron. 2015, 73, 47-63.
- (67) Xu, H.; Chen, J.; Birrenkott, J.; Zhao, J. X.; Takalkar, S.; Baryeh, K.; Liu, G. *Anal. Chem.* **2014**, *86*, 7351-7359.
- (68) Shen, G.; Xu, H.; Gurung, A. S.; Yang, Y.; Liu, G. *Anal. Sci.* **2013**, *29*, 799-804.
- (69) Horton, J. K.; Swinburne, S.; O'Sullivan, M. J. J. Immunol. Methods 1991, 140, 131-134.
- (70) Yang, W.; Li, X. B.; Liu, G. W.; Zhang, B. B.; Zhang, Y.; Kong, T.; Tang, J. J.; Li, D. N.; Wang, Z. *Biosens. Bioelectron.* **2011**, *26*, 3710-3713.
- (71) Fu, E.; Liang, T.; Houghtaling, J.; Ramachandran, S.; Ramsey, S. A.; Lutz, B.; Yager, P. *Anal. Chem.* **2011**, *83*, 7941-7946.
- (72) Kumar, M.; Kumar, R.; Bhalla, V. Org. Lett. **2010**, 13, 366-369.
- (73) Miao, P.; Ning, L.; Li, X. Anal. Chem. 2013, 85, 7966-7970.
- (74) Park, J.; Choi, S.; Kim, T. I.; Kim, T. Analyst 2012, 137, 4411-4414.
- (75) Hermanson, G. T. *Bioconjugate Techniques*, 2nd ed.; Academic Press: San Diego, 2008.
- (76) Beesley, J. E. Colloidal gold: A new perspective for cytochemical marking; Oxford University Press: Oxford, 1989.
- (77) Armbruster, D. A.; Tillman, M. D.; Hubbs, L. M. Clin. Chem. 1994, 40, 1233-1238.
- (78) Armbruster, D. A.; Pry, T. Clin. Biochem. Rev. 2008, 29, S49-S52.
- (79) Serp, P.; Philippot, K. *Nanomaterials in Catalysis*; John Wiley & Sons, Inc., **2013**.
- (80) Zhu, Z.; Guan, Z.; Liu, D.; Jia, S.; Li, J.; Lei, Z.; Lin, S.; Ji, T.; Tian, Z.; Yang, C. Angew.

- Chem. Int. Ed. 2015, 54, 10448-10453.
- (81) Rycenga, M.; Cobley, C. M.; Zeng, J.; Li, W.; Moran, C. H.; Zhang, Q.; Qin, D.; Xia, Y. *Chem. Rev.* **2011**, *111*, 3669-3712.
- (82) Lim, D.-K.; Jeon, K.-S.; Hwang, J.-H.; Kim, H.; Kwon, S.; Suh, Y. D.; Nam, J.-M. *Nat. Nanotechnol.* **2011**, *6*, 452-460.

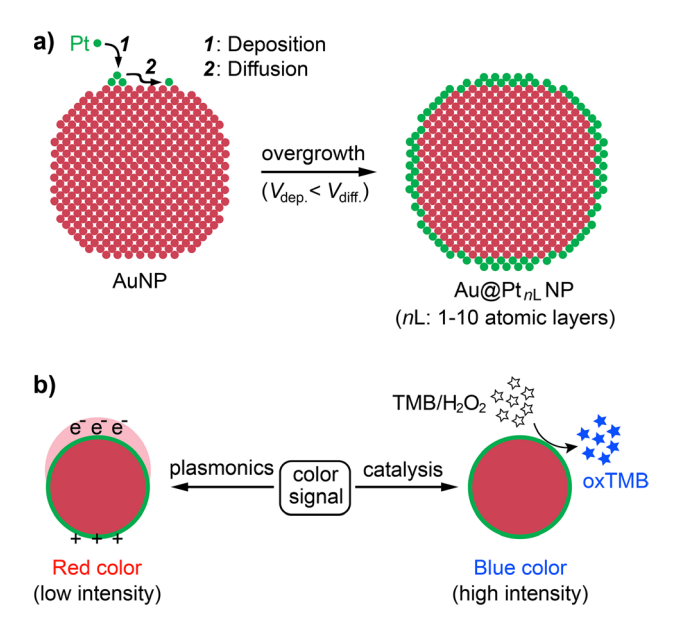


Figure 1. Schematics showing: (a) the fabrication of Au@Pt_{nL} NPs, in which Pt atoms are deposited onto an AuNP to form a conformal, thin Pt shell with thicknesses of 1-10 atomic layers; and (b) two types of color signal generated from Au@Pt_{nL} NPs under different mechanisms. In (a), the rate of atom deposition is controlled to be slower than that of surface diffusion ($V_{\text{dep.}} < V_{\text{diff.}}$).

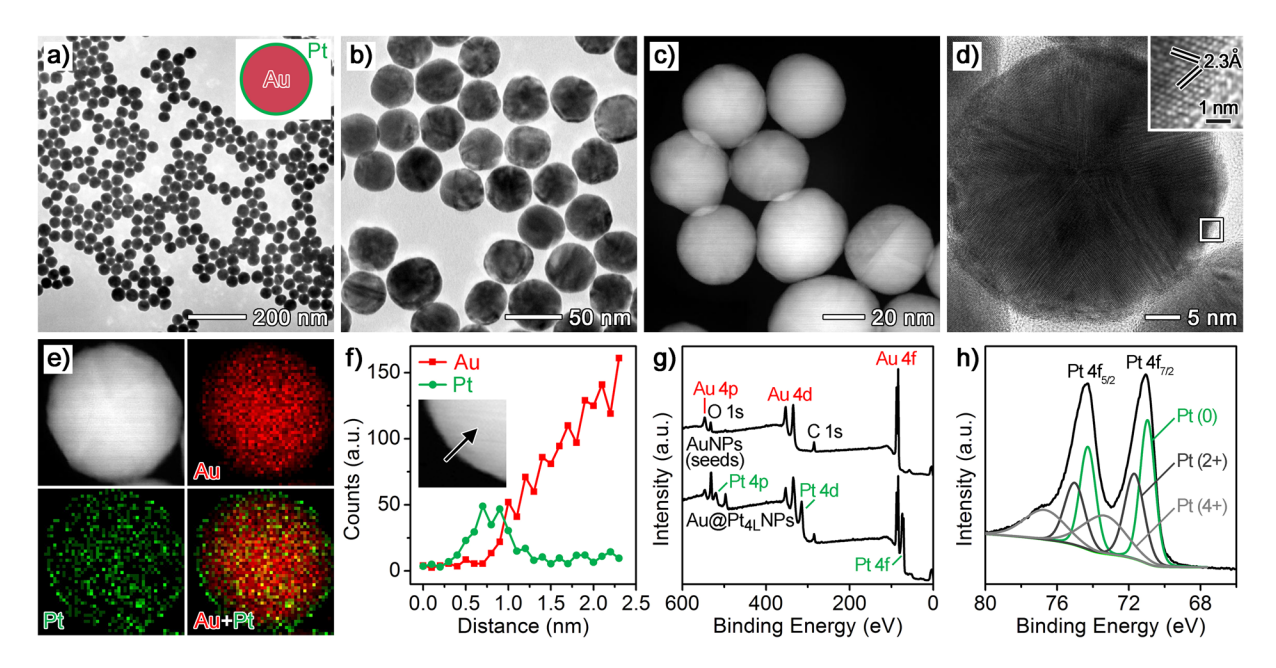


Figure 2. Morphological, structural, and compositional analyses of Au@Pt_{4L} NPs that were prepared from a standard synthesis. (a, b) TEM images at two different magnifications; (c) HAADF-STEM image; (d) High-resolution TEM image of an individual particle. Inset shows a magnified image of the region marked by a white box; (e) EDX mapping image of an individual particle (red = Au, green = Pt); (f) Line-scan EDX spectra of elemental Au and Pt that were recorded from an individual particle (inset) along a direction as indicated by the black arrow; (g) XPS survey spectra of the Au@Pt_{4L} NPs and initial AuNP seeds; (h) High-resolution XPS spectra of the Pt 4f region shown in (g).

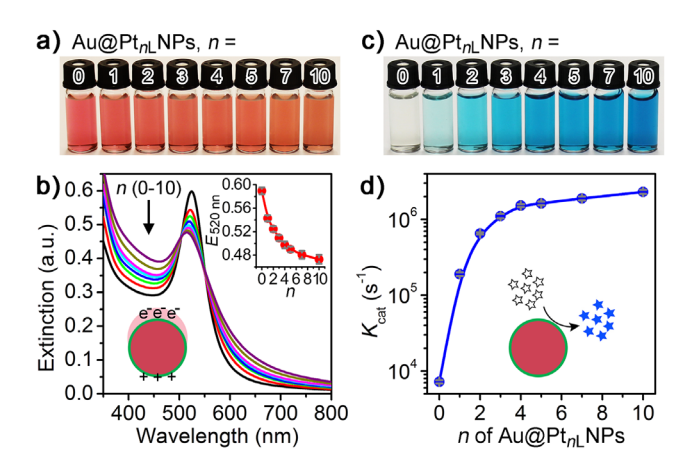


Figure 3. Plasmonic (a, b) and catalytic (c, d) properties of Au@Pt_{nL} NPs, where *n* denotes the number of Pt atomic layers (n = 0 corresponds to the initial AuNP seeds shown in Figure S1). (a) A photograph taken from aqueous suspensions of Au@Pt_{nL} NPs with the same particle concentration; (b) Corresponding UV-vis spectra recorded from the samples in (a). Inset shows a plot of extinction at 520 nm ($E_{520 \text{ nm}}$) against n; (c) A photograph taken from reaction solutions (*i.e.*, oxidation of TMB by H₂O₂) catalyzed by Au@Pt_{nL} NPs of the same particle concentration. In all measurements, the reaction time was fixed at t = 3 min. The blue color was originated from the oxidized TMB as the product ($\lambda_{\text{max}} = 653 \text{ nm}$). (d) A plot comparing the catalytic constant (K_{cat}) of different Au@Pt_{nL} NPs. Error bars in (b) and (d) indicate the standard deviations of three independent measurements.

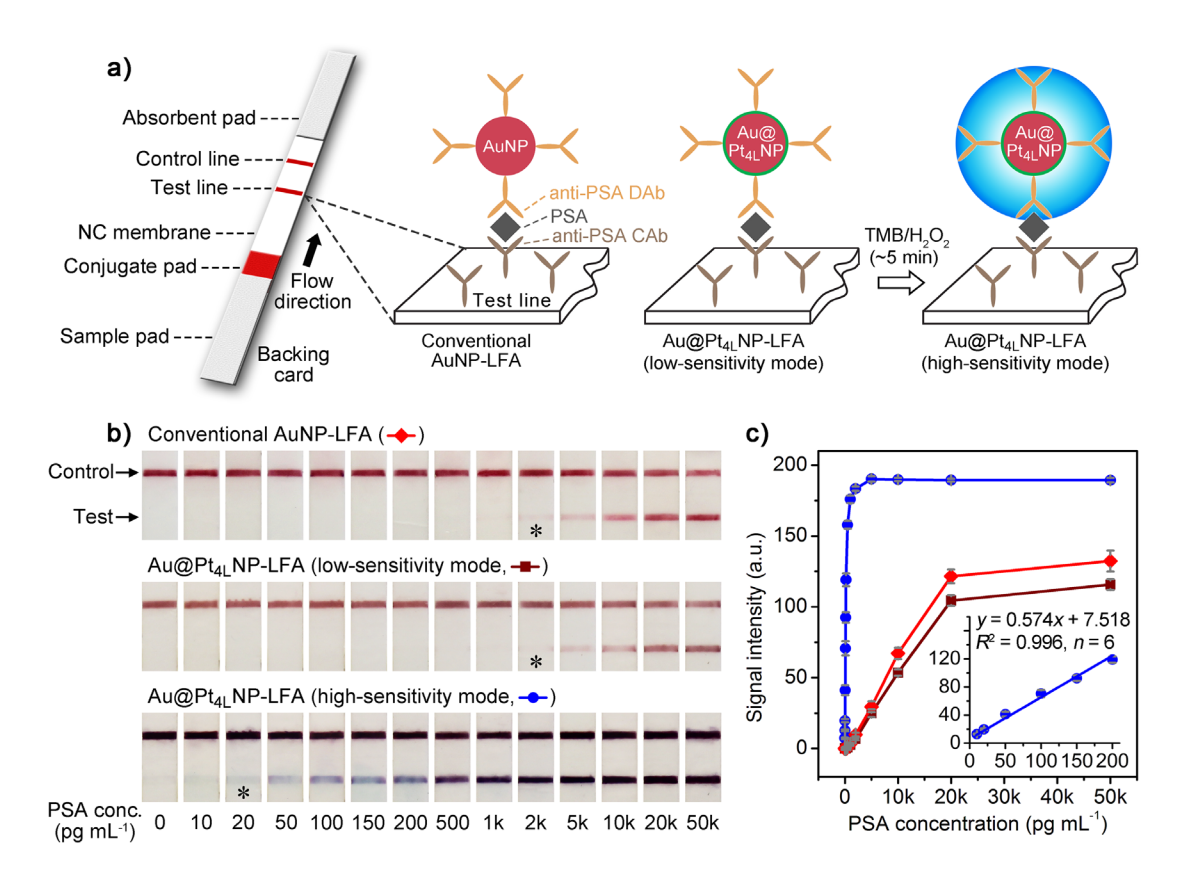


Figure 4. Detection of PSA with conventional AuNP-based LFA (AuNP-LFA) and Au@Pt4L NP-based LFA (Au@Pt4L NP-LFA). (a) Schematics showing the principles of AuNP-LFA and Au@Pt4L NP-LFA at low- and high-sensitivity modes (see Supporting Information for details about the preparation of LFAs); (b) Representative photographs taken from the LFAs of PSA standards. The asterisks (*) indicate detection limits by the naked eyes; (c) Corresponding calibration curves of the detection results shown in (b). Error bars indicate the standard deviations of six independent measurements. Inset shows the linear range region of the Au@Pt4L NP-LFA at high-sensitivity mode.

Table 1. The performances of Au@Pt_{4L} NP-LFA (high-intensity mode) and a commercial ELISA kit (Abcam plc., United Kingdom) in detecting PSA spiked human plasma samples.

	PSA amount spiked (pg mL ⁻¹)	PSA amount measured (pg mL ⁻¹)	Coefficient of variations (%, n = 6)	Recovery (%)
Au@Pt _{4L} NP-LFA	20	18.9	7.3	94.5
	40	38.7	5.2	96.8
	80	76.9	6.2	96.1
	120	127.9	4.1	106.6
	160	163.4	5.1	102.1
Commercial ELISA kit	20	18.4	3.6	92.0
	40	40.5	2.6	101.3
	80	82.3	3.3	102.9
	120	116.2	2.6	96.8
	160	157.6	3.1	98.5